The Astrophysical Journal, 817:22 (8pp), 2016 January 20 doi:10.3847/0004-637X/817/1/22

PROBING FINAL STAGES OF STELLAR EVOLUTION WITH X-RAY OBSERVATIONS OF SN 2013ej

Sayan Chakraborti[1,11], Alak Ray[1,12], Randall Smith[2], Raffaella Margutti[3], David Pooley[4], Subhash Bose[5], Firoza Sutaria[6], Poonam Chandra[7], Vikram V. Dwarkadas[8], Stuart Ryder[9], and Keiichi Maeda[10]
[1] Institute for Theory and Computation, Harvard-Smithsonian Center for Astrophysics, 60 Garden Street, Cambridge, MA 02138, USA; schakraborti@fas.harvard.edu
[2] Harvard-Smithsonian Center for Astrophysics, 60 Garden Street, Cambridge, MA 02138, USA
[3] Center for Cosmology and Particle Physics, New York University, 4 Washington Place, New York, NY 10003, USA
[4] Department of Physics and Astronomy, Trinity University, San Antonio, TX 78212, USA
[5] Aryabhatta Research Institute of Observational Sciences, Manora peak, Nainital, India
[6] Indian Institute of Astrophysics, Koramangala, Bangalore, India
[7] National Centre for Radio Astrophysics, Pune University Campus, Pune 411 007, India
[8] Department of Astronomy and Astrophysics, University of Chicago, 5640 S Ellis Avenue, Chicago, IL 60637, USA
[9] Australian Astronomical Observatory, P.O. Box 915, North Ryde, NSW 1670, Australia
[10] Department of Astronomy, Kyoto University, Kitashirakawa-Oiwake-cho, Sakyo-ku, Kyoto 606-8502, Japan
Received 2015 October 19; accepted 2015 November 19; published 2016 January 19

ABSTRACT

Massive stars shape their surroundings with mass loss from winds during their lifetimes. Fast ejecta from supernovae (SNe), from these massive stars, shock this circumstellar medium. Emission generated by this interaction provides a window into the final stages of stellar evolution, by probing the history of mass loss from the progenitor. Here we use *Chandra* and *Swift* X-ray observations of the type II-P/L SN 2013ej to probe the history of mass loss from its progenitor. We model the observed X-rays as emission from both heated circumstellar matter and SN ejecta. The circumstellar density profile probed by the SN shock reveals a history of steady mass loss during the final 400 years. The inferred mass loss rate of $3 \times 10^{-6}\,M_{\odot}\,\mathrm{yr}^{-1}$ points back to a 14 $M_{\odot}$ progenitor. Soon after the explosion we find significant absorption of reverse shock emission by a cooling shell. The column depth of this shell observed in absorption provides an independent and consistent measurement of the circumstellar density seen in emission. We also determine the efficiency of cosmic ray acceleration from X-rays produced by Inverse Compton scattering of optical photons by relativistic electrons. Only about 1% of the thermal energy is used to accelerate electrons. Our X-ray observations and modeling provide stringent tests for models of massive stellar evolution and micro-physics of shocks.

Key words: circumstellar matter – shock waves – stars: mass-loss – supernovae: individual (SN 2013ej) – X-rays: general

1. INTRODUCTION

One of the central problems in astrophysics is the mapping of stellar properties onto the properties of supernovae (SNe) that they may or may not produce. Mass, spin, metallicity, and binarity are some of the parameters which are thought to determine the final outcome of stellar evolution (Heger et al. 2003).

SNe II-P are produced by red supergiants, between 8 and 17 $M_{\odot}$ in mass (Smartt et al. 2009). X-ray lightcurves of SNe II-P point to an upper limit of 19 $M_{\odot}$ for their progenitors (Dwarkadas 2014). Yet not all stars with such masses necessarily give rise to SNe II-P. In the final stages of stellar evolution the cores of massive stars rapidly burn through elements of progressively higher atomic numbers (Weaver et al. 1978). This may cause rapid variation in the energy output of the core. However, the outer layers of these stars need approximately a Kelvin–Helmholtz timescale ($\sim 10^6$ years) to adjust to these changes. Therefore, surface properties like luminosity and mass loss rate should not change on short timescales in direct response. However recent observations of luminous outbursts and massive outflows from Luminous Blue Variable progenitors (Smith et al. 2010) months to years before certain SNe, like SN 2009ip (Mauerhan et al. 2013; Ofek et al. 2013; Pastorello et al. 2013; Margutti et al. 2014), call this paradigm into question (Smith 2014).

The pre-supernova evolution of massive stars shape their environments by winds and ionizing radiation. The interaction of the SN ejecta with this circumstellar matter produces radio and X-ray emission. Our ongoing program (Chakraborti et al. 2012; Chakraborti et al. 2013) is to observe these X-rays using various sensitive instruments and model their emission mechanism. In this work, we use *Chandra* and *Swift* X-ray observations of SN 2013ej to probe the history of mass loss from its progenitor during the last 400 years before explosion. At early times we find significant absorption of reverse shock emission by a cooling shell. We also determine the efficiency of cosmic ray acceleration from X-rays produced by Inverse Compton scattering of optical photons by relativistic electrons. Our results demonstrate that sensitive and timely X-ray observations of young nearby SNe, coupled with modeling of the emission and absorption produced by shocked plasmas, provide stringent tests for models of pre-supernova massive stellar evolution.

2. OBSERVATIONS OF SN 2013EJ

SN 2013ej exploded in the nearby galaxy M74 (Dhungana et al. 2013; Kim et al. 2013; Valenti et al. 2013; Waagen et al. 2013) and was observed in multiple bands. It was initially classified as a SN II-P (Lee et al. 2013; Leonard et al. 2013; Richmond 2014) with a slow rise (Valenti et al. 2014), but due

[11] Society of Fellows, Harvard University, 78 Mount Auburn Street, Cambridge, MA 02138, USA.
[12] Present Address: Tata Institute of Fundamental Research, 1 Homi Bhabha Road, Colaba, Mumbai 400 005, India.

Table 1
Swift and *Chandra* Observations of SN 2013ej

Dates (2013)	Age[a] (days)	L_{bol} (erg s^{-1})	Telescope	Exposure (ks)	X-ray Flux (0.5–8 keV) (erg cm^{-2} s^{-1})
Jul 30–Aug 9	13.0	$(3.89 \pm 0.58) \times 10^{42}$	*Swift*	73.4	$(7.1 \pm 1.2) \times 10^{-14}$
Aug 21	28.9	$(2.19 \pm 0.27) \times 10^{42}$	*Chandra*	9.8	$(9.8 \pm 3.2) \times 10^{-15}$
Sep 21	59.7	$(1.29 \pm 0.03) \times 10^{42}$	*Chandra*	39.6	$(1.0 \pm 0.2) \times 10^{-14}$
Oct 7–11	78.0	$(1.00 \pm 0.02) \times 10^{42}$	*Chandra*	38.4	$(7.0 \pm 1.0) \times 10^{-15}$
Nov 14	114.3	$(8.13 \pm 0.38) \times 10^{40}$	*Chandra*	37.6	$(7.0 \pm 1.3) \times 10^{-15}$
Dec 15	145.1	$(5.13 \pm 0.24) \times 10^{40}$	*Chandra*	40.4	$(4.8 \pm 0.8) \times 10^{-15}$

Notes. The *Chandra* observations can be retrieved from the *Chandra* Data Archive using their Obs Ids of 14801, 16000, 16001 (with fragments in 16484 and 16485), 16002, and 16003.
[a] Age at the middle of an observation with an assumed explosion date 2013 July 23.8 (UT) (JD 2456497.3 ± 0.3) following Bose et al. (2015).

to its fast decline (Huang et al. 2015) it was later re-classified as a SN II-L (Bose et al. 2015; Valenti et al. 2015). Sanders et al. (2015) have shown that SNe of type II-P and II-L form a continuum of lightcurve properties like plateau duration. SN 2013ej falls somewhere along this continuum. In this work we adopt a distance of $d \sim 9.57 \pm 0.70$ Mpc and an explosion date of 2013 July 23.8 (Bose et al. 2015). Details of the X-ray observations, carried out by us and used in this work, are given below and in Table 1.

2.1. Swift XRT Observations

The *Swift* XRT observed SN 2013ej in X-ray bands starting from 2013 July 30 until 2013 July 31. Margutti et al. (2013) analyzed and reported data collected during the first 15 ks of observations. The X-ray counterpart of SN2013ej was found to be separated from nearby sources. The significance of the X-ray source detection in the *Swift* observation was 5.2 sigma. In this work we use X-ray data collected over a longer duration of 73.4 ks by the XRT. The X-ray counterpart of SN2013ej, as seen by the XRT, is 45″ away from a ULX source M74 X-1 which is clearly detected and resolved. It is also 15″ from an X-ray source J013649.2+154527 observed by *Chandra*. These circumstances make follow-up *Chandra* observations with superior angular resolution particularly important.

2.2. Chandra X-Ray Observations

After the initial detection by *Swift*, we triggered our Target of Opportunity observations with the *Chandra* X-ray Observatory for five epochs. The first *Chandra* observation was approximately 10 ks and the four subsequent observations were all ∼40 ks each. All exposures were carried out using *Chandra* ACIS-S CCDs without any grating. The details of observations of SN 2013ej with *Swift* and *Chandra* X-ray instruments are given in Table 1. These data from each epoch of observations were processed separately, but identically. The spatial and spectral analyses were performed after this initial processing by following the prescription[13] from the *Chandra* Science Center using CIAO 4.7 with CALDB 4.6.9.

The initial data processing steps were identical to that of SN 2004dj (Chakraborti et al. 2012) and SN 2011ja (Chakraborti et al. 2013). Photons recorded in level 2 events were filtered by energy to select only those above 0.3 keV and below 10 keV. The selected photons were projected back onto sky coordinates and the emission from the SN was easily identified. The portion of the sky containing the SN was masked and a light curve was generated from the remaining counts. Cosmic ray induced flares were identified in this light curve, using times where the count rate flared 3σ above the mean. A good time interval table was generated by excluding these flares. This was used to further select photons from the useful exposure times reported in Table 1. The spectra, response matrices, and background count rates were then generated from these filtered photons. To retain the highest available spectral resolution, we did not bin these data. All subsequent steps use this processed data.

[13] The method for extraction of spectrum and response files for an unresolved source is described in http://cxc.harvard.edu/ciao/threads/pointlike/

3. MODELING THE X-RAYS

The expansion of fast SN ejecta drives a strong forward shock into circumstellar matter (Chevalier 1974) and heats it to ∼100 keV. The expansion also causes rapid adiabatic cooling in the ejecta. However, an inward propagating reverse shock is generated by the deceleration of the ejecta by the ambient medium (McKee 1974), reheating it to ∼1 keV or even higher. We use thermal and non-thermal emission processes, as well as absorption, occurring in these shocked regions to model X-rays observed (Figure 1) from SN 2013ej. Note that the hard X-ray flux, initially the dominant part, rapidly declines and beyond ∼40 days the total flux is dominated by the soft X-ray flux. The observed spectrum (Figure 2) is represented as the sum of these emission components, passed through the appropriate absorption components and folded in with the relevant response matrices. The XSPEC model we used is tbabs (tbabs(apec) + bremss + powerlaw). Here external absorption is modeled by the first tbabs and internal by the second one. The apec component represents thermal emission from reverse shock while the bremss represents that from forward shock. The Inverse Compton component is represented by powerlaw.

3.1. Thermal Emission

The reverse shock climbs up against the steep ejecta profile of the SN and therefore encounters larger densities than the forward shock. The temperature of the reverse shock can in many cases be right where *Chandra* is most sensitive. Therefore thermal emission from the reverse shock is likely to be the dominant component at late times beyond a month (Chakraborti et al. 2012). The thermal emission from the forward shock can become important if the emission from the reverse shock is absorbed.

The thermal X-rays from the reverse shock are composed of bremsstrahlung and line emission. Nymark et al. (2006) used

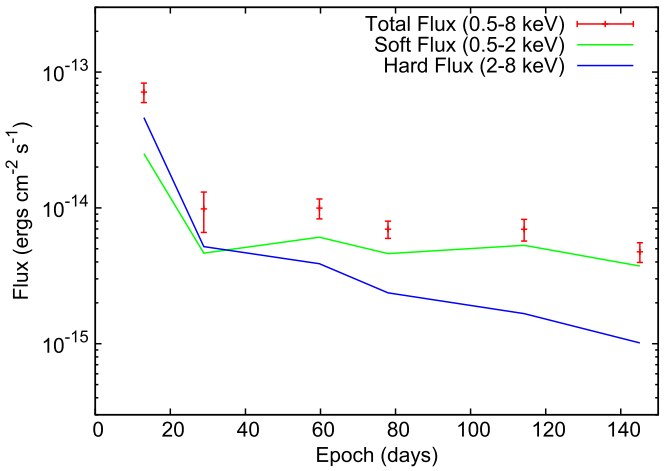

Figure 1. X-ray fluxes observed from SN 2013ej. Total fluxes (red, with 1σ uncertainties) can be split into soft (green) and hard (blue) components. Note that the hard component dominates at first. However, it drops off rapidly as the Inverse Compton flux dies off and the thermal plasmas become cooler. The soft component does not drop off as rapidly, because the reduced emission is somewhat offset by reduced absorption at late times.

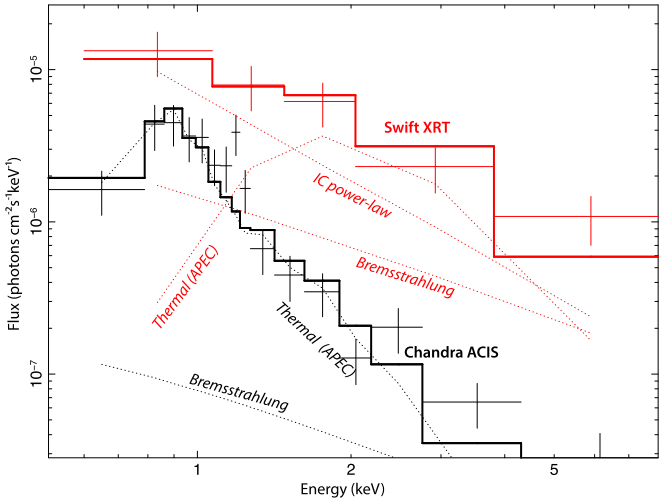

Figure 2. Unfolded X-ray spectra of SN 2013ej from *Swift* XRT at early times (in red) and *Chandra* ACIS at later times (in black) with 1σ uncertainties. The *Swift* spectrum represents the earliest epoch and has comparable contribution from thermal reverse shock emission, thermal forward shock emission and Inverse Compton scattering. The later time *Chandra* spectra from 5 epochs listed in Table 1, are stacked together only for display but analyzed separately. Note that the late time *Chandra* spectra are softer than the early time *Swift* spectrum. The *Chandra* spectra are dominated by thermal emission from the reverse shock.

time-dependent ionization balance and multilevel calculations to model the line emission from the reverse shock. Chakraborti et al. (2012) have shown that it is safe to assume collisional ionization equilibrium while trying to model the line emission from the reverse shocked material. The strengths of lines from a plasma in equilibrium can be determined from its temperature and composition. We use the APEC code (Smith et al. 2001) to model the thermal emission from the reverse shock.

The thermal emission from the forward shock is modeled simply as bremsstrahlung radiation with a normalization of $N_{\rm bremss}$. We expect it to be too tenuous and hot to produce any significant lines in the *Chandra* or XRT bands (Chakraborti et al. 2012).

3.2. Non-thermal Emission

The forward shocks, apart from heating the circumstellar material, also accelerate cosmic rays. The relativistic electrons at the forward shock lose energy via synchrotron emission, which is detected in the radio (Chevalier 1982b), and Inverse Compton scattering of optical photons into the X-rays (Chakraborti et al. 2012). Here we model the Inverse Compton emission as a power law in XSPEC with a normalization of $N_{\rm IC}$. An electron population described by a power law with index p generates Inverse Compton scattered X-rays with a photon index $(p + 1)/2$.

3.3. Absorption Components

We consider two absorption components, both modeled using the Tuebingen-Boulder ISM absorption model (Wilms et al. 2000). We consider the external absorption to be a constant in time as it is likely produced by material far away from the SN. Radiative cooling of the reverse shocked material leads to the formation of a dense cool shell (Chevalier & Fransson 2003, pp. 171–194) which can obscure the emission from the reverse shock. We model this as a time-varying internal absorption component.

4. X-RAY SPECTRAL FITTING

All X-ray data are loaded into XSPEC and fitted in the manner described in Chakraborti et al. (2012). Since these data are unbinned, individual spectral channels can have a low number of photons, disallowing the use of a χ^2 statistic. We therefore adopt the W statistic generalization of the Cash (1979) statistic. We need to fit 6 epochs with 10 parameters each. Since there is not enough information in the observed spectra to simultaneously determine all 60 parameters, it is necessary to hold some of them constant or constrained. We describe these restricted parameters below. All fitted parameters are reported in Table 2.

4.1. Constant Parameters

Bose et al. (2015) find no excess reddening in the optical emission from SN 2013ej beyond what is expected from the Galactic absorption. We therefore hold the external absorption column constant, at the Galactic value of $n_{\rm ext} = 4.8 \times 10^{20}$ atoms cm^{-2} determined from the Leiden Argentine Bonn (LAB) Survey of Galactic H I (Kalberla et al. 2005).

A visual inspection of the spectra reveals a bump at $\sim$1 keV, which is likely produced by a blend of lines, but not enough resolved features to determine the metallicity of the plasma. We therefore set the relative metal abundances in APEC following Asplund et al. (2009). The overall metallicity is set to $Z = 0.295 Z_{\odot}$, which is equal to that of the nearby H II region number 197 of Cedrés et al. (2012). In the absence of prominent sharply resolved lines, the redshift cannot be determined from the spectra. We therefore fix it to the host galaxy redshift of $z = 2.192 \times 10^{-3}$ from NED.

The early spectrum at the first epoch is hard, with a possible contribution from Inverse Compton scattering. But there is unlikely to be enough information to be able to determine the slope of this component. We therefore fix the photon index to $\alpha_{\rm IC} = 2$, which is expected on theoretical grounds for an electron index of $p = 3$ and has been observed in SN 2004dj (Chakraborti et al. 2012).

Table 2
Spectral Fits to X-ray Observations of SN 2013ej

	Model Parameters						Derived Quantities	
t_{obs} (days)	N_{IC} (ph keV^{-1} cm^{-2} s^{-1})	T_{cs} (keV)	N_{bremss}	n_{cool} (10^{22} cm^{-2})	T_{rev} (keV)	N_{APEC} (10^{-5})	t_{look} (yr)	$\dot{M}$ ($10^{-6}\,M_{\odot}$ yr^{-1})
13.0 ± 5.8	(6.5 ± 2.7) × 10^{-6}	…	…	4 ± 1	1.13 ± 0.25	30.8 ± 15.7	48 ± 17	4.38 ± 1.53
28.9 ± 0.3	…	…	…	…	…	2.16 ± 1.66	79 ± 5	1.67 ± 0.65
59.7 ± 0.4	…	…	…	…	…	3.25 ± 1.37	152 ± 9	2.83 ± 0.64
78.0 ± 1.8	…	…	…	…	…	2.06 ± 0.82	193 ± 12	2.54 ± 0.55
114.3 ± 0.4	…	…	…	…	…	2.00 ± 0.70	272 ± 16	2.98 ± 0.58
145.1 ± 0.4	…	…	…	…	…	0.82 ± 0.43	338 ± 19	2.61 ± 0.50
Scalings for … Entries								
	$\propto L_{bol} t^{-1}$		$=81T_{rev}$	$=0.0228N_{APEC}$	$\propto t^{-1}$	$\propto t^{-1/5}$		

Note. Free model parameters are determined from fits. Entries marked with … are not frozen. They are allowed to vary, but only in proportion to other parameters as described in Section 4.2. Apart from the 6 columns of model parameters listed above, each epoch also has 4 other parameters which are held constant and are identical at each epoch. These parameters are the external absorbing column density $n_{ext} = 4.8 \times 10^{20}$ atoms cm^{-2}, powerlaw slope for the Inverse Compton component $\alpha_{IC} = 2$, redshift $z = 2.192 \times 10^{-3}$, and metallicity $Z = 0.295 Z_{\odot}$. The motivations for fixing the parameters to these particular values are described in Section 4.1. The norms for the bremss and apec components are reported in the units used inside XSPEC, so that readers can reproduce the model easily. The lookback time and mass loss rates are derived from the model parameters, for a progenitor wind velocity of $v_w = 10$ km s^{-1}.

4.2. Constrained Parameters

Here we constrain various parameters which determine how the shape of the spectra change in time. To derive these relations, we assume a steady mass loss rate from the progenitor. If the mass loss is significantly variable, the data will rule out the model. We allow the absorption column depth of the cool shell to be determined by the best-fit to these data. However, the value of relative depth of the column at six epochs are tied to each other using the relation

$$n_{cool} \propto t^{-1} \quad (1)$$

from Chevalier & Fransson (2003, pp. 171–194). This removes five free parameters.

At each epoch the temperature of the forward shock can be related to that of the reverse shock. Using the self similar solution for a SN ejecta interacting with a steady wind (Chevalier 1982a), we find

$$T_{cs} = (n-3)^2 T_{rev}, \quad (2)$$

where n is the power law index of the ejecta profile. Following Matzner & McKee (1999) we use $n = 12$, as is appropriate for a red supergiant progenitor. Fixing the forward shock temperature to be 81 times the reverse shock temperature at each of the epochs removes six free parameters. The temperature of the reverse shocked plasma also goes down slowly in time as

$$T_{rev} \propto t^{-\frac{2}{n-2}}. \quad (3)$$

The temperature of the apec component at one epoch is therefore allowed to vary but its values at all other epochs are linked to each other using this proportionality. This removes five more free parameters.

The emission measures of the plasma at the forward and reverse shocks can be similarly related. Self similar solutions Chevalier & Fransson (2003, pp. 171–194) provide the physical relation between the emission measures as

$$\int n_e n_H dV_{rev} = \frac{(n-3)(n-4)^2}{4(n-2)} \int n_e n_H dV_{cs}. \quad (4)$$

Two more factors arise because we are forced to use two different models for the emissions, namely APEC and bremsstrahlung. In XSPEC, the APEC model (Smith et al. 2001) represents the emission measure as $\int n_e n_H dV$, whereas the bremss model (Kellogg et al. 1975) uses $\int n_e n_I dV$. To resolve this, we approximate $n_I = n_H + n_{He}$ with the helium abundance from Asplund et al. (2009). Furthermore, there is an arbitrary numerical difference in the normalizations of the models. Accounting for these three issues, we set the bremss norm N_{bremss} to be 0.0228 times the APEC norm N_{APEC} at each epoch. This eliminates another six free parameters.

Only the earliest epoch is likely to have significant contribution from Inverse Compton scattering of optical photons by relativistic electrons. Chevalier & Fransson (2006) have shown that the Inverse Compton flux is expected to fall off as

$$N_{IC} \equiv E \frac{dL_{IC}}{dE} \propto L_{bol} t^{-1}, \quad (5)$$

where L_{bol} is the bolometric luminosity of the SN which provides the seed photons to be up-scattered. We relate the norm of the powerlaw component, representing the Inverse Compton emission, at all later epochs to that of the first epoch using this relation. To estimate the bolometric luminosity before 30 days, we use the B and V band luminosities from Richmond (2014) and the bolometric correction prescribed by Bersten & Hamuy (2009). Beyond 30 days, we use the bolometric luminosity reported in Bose et al. (2015) by integrating the emission from the infrared to ultraviolet. All the bolometric luminosities used are reported in Table 1.

4.3. Goodness and Uncertainties

Having obtained the best fit, we tested the goodness of the fit by generating a set of 1000 simulated spectra, at each epoch, with a parameter distribution that is derived from the covariance matrix of parameters at the best fit. We note that goodness testing is a misnomer for this process as it can never determine whether a particular fit is good, only if it is

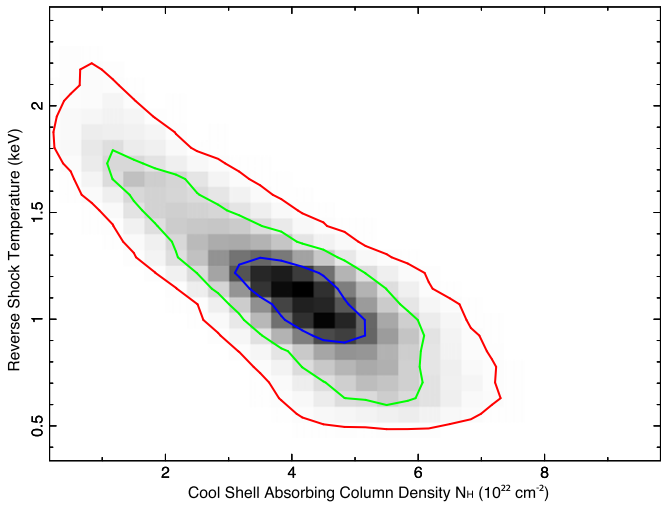

Figure 3. Correlation between cool shell absorption column depth and reverse shock plasma temperature at the first epoch. 1 (blue), 2 (green) and 3 (red) σ uncertainty contours are obtained by marginalizing the results of our MCMC run. A larger absorbing column can hide lower energy emission from a cooler reverse shocked plasma, giving rise to the negative correlation. The closed 3σ contour demonstrates that even with the uncertainty in the reverse shock temperature we need a non-zero column depth in the cooling shell absorption component at the 3σ.

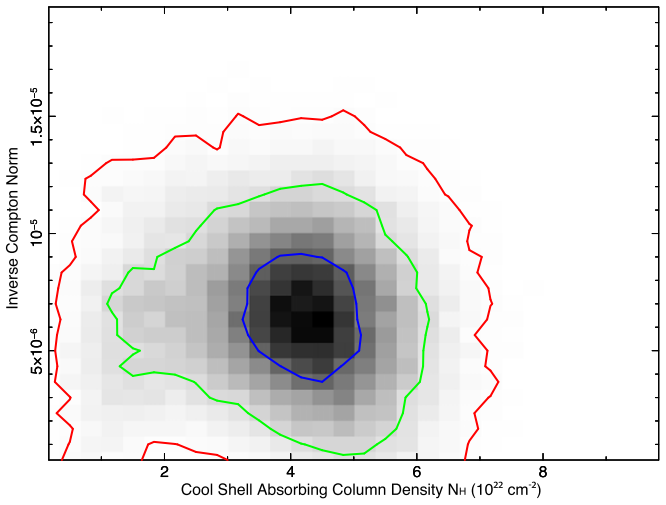

Figure 4. Correlation between cool shell absorption column depth and Inverse Compton emission at the first epoch. 1 (blue), 2 (green) and 3 (red) σ uncertainty contours are obtained by marginalizing the results of our MCMC run. A larger absorbing column can hide reverse shock emission allowing harder forward shock emission to dominate the spectrum. This makes the thermal contribution to the spectrum harder and therefore requires less Inverse Compton emission to explain the high energy photons, giving rise to the negative correlation. The closed 2σ contour demonstrates that after marginalizing over the uncertainties in the thermal components, we need a non-zero contribution from the non-thermal Inverse Compton component at the 2σ level.

significantly bad or not. Only 60% of these sets of fake data have a fit statistic better than the fiducial fit. If the observations were indeed generated by the model the most likely percentage, of fake data that have a fit statistic better than the fiducial fit, is 50. However, the likelihood of the percentage lying outside the range of 40%–60% is 0.8. Since the outcome of the goodness test is quite likely, our data do not rule out the model. We therefore consider the model to be acceptable.

In order to better understand the uncertainties in the determined parameters we ran a Markov Chain Monte Carlo simulation. Two hundred walkers were initiated using the fit covariance matrix as the proposal distribution. They were allowed to walk for 400,000 steps, after rejecting the first 40,000 steps. They were evolved following the Goodman–Weare algorithm (Hou et al. 2012) implemented in XSPEC (Arnaud 2013). The uncertainties for each parameter were determined by marginalizing over all other parameters. Two pairs of parameters were found to have noteworthy correlations and are discussed below.

The uncertainty in the column depth of the cool shell influences the uncertainties in the reverse shock temperature (see Figure 3) and the Inverse Compton flux density (see Figure 4). A heavier absorbing column can hide the lower energy emission from a colder plasma, leading to the negative correlation with the reverse shock temperature. A heavier absorbing column, having hidden much of the reverse shock emission, also allows for a larger hot bremsstrahlung contribution from the forward shock. This explains away more of the harder photons, thus requiring a lesser contribution from the Inverse Compton component. This causes the column depth to be also negatively correlated with the Inverse Compton flux.

5. RESULTS

We interpret the plasma parameters determined from the model fits to our observations in terms of a physical description of the SN and its progenitor.

5.1. Shock Velocity

Chevalier (1982b) related the temperature of the forward shocked material with the shock velocity. Nymark et al. (2006) used this to derive the temperature of the reverse-shocked material in terms of the forward shock velocity. The reverse shocked plasma is expected to be dense enough (Chakraborti et al. 2012) to reach ionization equilibrium. Under such conditions, Chakraborti et al. (2012) have inverted this relation to express the forward shock velocity, which is a property of the SN explosion, to the reverse shock temperature which is an observable, as

$$V_{\rm cs} = 10^4 \sqrt{\frac{kT_{\rm rev}}{1.19\ {\rm keV}}}\ \ {\rm km\ s^{-1}}. \quad (6)$$

Since the best-fit temperature is 1.1 ± 0.2 keV (see Figure 3), the implied velocity at 12.96 days is $V_{\rm cs} = (9.7 \pm 1.1) \times 10^3$ km s^{-1}. This is faster than the shock velocity observed in SN 2004dj (Chakraborti et al. 2012). Also, note that the forward shock is expected to be faster than the photosphere. As expected, $V_{\rm cs}$ here is faster than velocities seen in optical linewidths (Bose et al. 2015).

5.2. Mass Loss History

Mass loss from the progenitor sets up the circumstellar density within which the SN interacts. The circumstellar density determines the emission measure of the forward shocked material. This can be related to the emission measure of the reverse shocked material using self similar solutions (Chakraborti et al. 2012). Considering only the contribution of hydrogen and helium to the mass and number density of the outermost shells of the SN, $\rho = 1.17$ amu $\times\ n_{\rm e} = 1.34$ amu $\times\ n_{\rm H}$. Therefore we modify the emission measure derived by Chakraborti

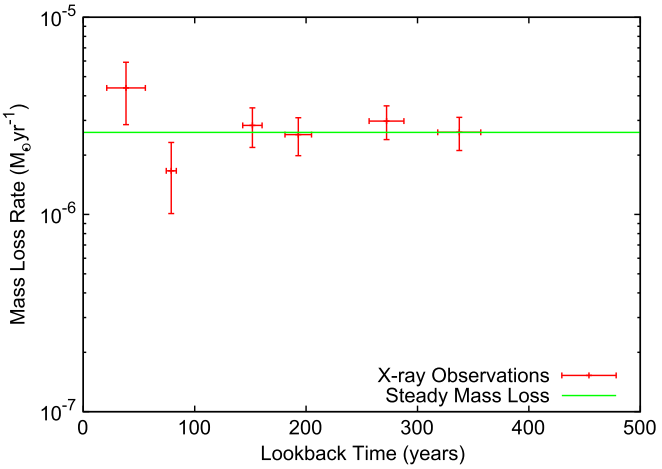

Figure 5. Pre-supernova mass loss rate from the progenitor as a function of time before explosion with 1σ uncertainties. The mass loss rates are derived using thermal emission from shocked plasma measured in the X-rays. Note that our measurements are consistent with a steady mass loss rate of $\dot{M} = (2.6 \pm 0.2) \times 10^{-6}\, M_\odot\ \mathrm{yr}^{-1}$ for the last 400 years of pre-supernova stellar evolution.

et al. (2012) for the reverse-shocked material as

$$\int n_e n_H dV = \frac{(144/\pi)\left(\dot{M}/v_w\right)^2}{(1.17\ \mathrm{amu})(1.34\ \mathrm{amu})R_{cs}}. \quad (7)$$

Only half of this emission measure contributes to the observed flux, as the other half is absorbed by the opaque unshocked ejecta. The norm of apec in XSPEC is defined as

$$N_{APEC} = \frac{10^{-14}}{4\pi\left(D_A(1+z)\right)^2}\int n_e n_H dV, \quad (8)$$

where D_A is the angular diameter distance to the source. Therefore, the mass loss rate can now be determined from the emission measure as

$$\dot{M} = 7.5 \times 10^{-7}\left(\frac{v_w}{10\ \mathrm{km\ s^{-1}}}\right)\left(\frac{D_A(1+z)}{10\ \mathrm{Mpc}}\right) \times \left(\frac{N_{APEC}}{10^{-5}}\right)^{1/2}\left(\frac{R_{cs}}{10^{15}\ \mathrm{cm}}\right)^{1/2} M_\odot\ \mathrm{yr}^{-1}. \quad (9)$$

We determine the norm of the APEC emission measure directly from our fit. We calculate the radius from the velocity determined in the last section and the time of observation. We assume a wind velocity $v_w = 10$ km s^{-1} as is appropriate for red supergiant progenitors.

The emission measures determined at various times after the explosion, point back to mass loss rates at different lookback times before the explosion. These are plotted in Figure 5 as a function of the lookback time t_{look}. Note that our observations are consistent with a $\propto r^{-2}$ density profile as expected from a steady mass loss rate of $\dot{M} = (2.6 \pm 0.2) \times 10^{-6} \times (v_w/10\ \mathrm{km\ s^{-1}})\, M_\odot\ \mathrm{yr}^{-1}$ over the last $400 \times (v_w/10\ \mathrm{km\ s^{-1}})^{-1}$ years of pre-supernova stellar evolution.

We compare this observed mass loss rate of the progenitor of SN 2013ej with what is expected from theory. MESA (Paxton et al. 2011) was used to simulate stars with masses between 11 to 19 $M_\odot$, for half solar metallicity. Paxton et al.'s (2011)

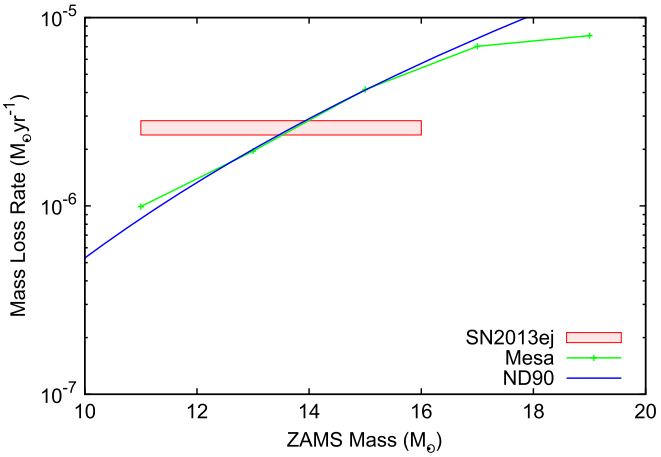

Figure 6. Zero Age Main Sequence Mass (ZAMS) and wind mass loss rate for MESA runs (green), and theoretical line (blue) from Nieuwenhuijzen & de Jager (1990) plotted for comparison. Shaded box represents 1σ confidence intervals for mass loss rate observed in SN 2013ej ($\dot{M} = (2.6 \pm 0.2) \times 10^{-6}\, M_\odot\ \mathrm{yr}^{-1}$, see Figure 5 of this work) and the estimated progenitor mass (11–16 $M_\odot$, from literature). Note that the observed mass loss is consistent with the theoretical expectations of mass loss rates from red supergiant stars (Nieuwenhuijzen & de Jager 1990). Our mass loss rate measurement points back to a more precise estimate of the progenitor mass, $M_{ZAMS} = 13.7 \pm 0.3\, M_\odot$.

Section 6.6 describe the mass loss prescription used in our simulations as the *Dutch* Scheme. We expect the SN ejecta to encounter the mass lost during the red giant branch phase of the wind which follows de Jager et al. (1988). In Figure 6 we compare the observed mass loss rate with those obtained from MESA and from Nieuwenhuijzen & de Jager (1990) for a progenitor size of $10^3 R_\odot$. Note however that various modifications have been suggested to this prescription (Mauron & Josselin 2011).

We consider a progenitor mass ranging from 11 to 16 $M_\odot$ combining pre-supernova progenitor identification (Fraser et al. 2014) and modeling of the SN lightcurve (Bose et al. 2015; Dhungana et al. 2015). Within this mass range, the mass loss rate obtained from X-ray observations in this work are in agreement with the predictions from both MESA and Nieuwenhuijzen & de Jager (1990).

5.3. Cooling Shell Absorption

Chevalier & Fransson (2003, pp. 171–194) proposed that a shell of material formed by the radiative cooling of shocked material may form between the reverse and forward shocked materials. Though more material is cooled with time, it gets diluted with the expansion of the ejecta. Also, as the density of the reverse shocked material falls, it does not cool as effectively as before. Therefore, this shell poses larger absorbing column densities at early times. Since the emission from the reverse shocked material is softer, hiding some of it makes the total spectrum harder. We determine the column density of this cold material at 12.96 days to be $n_{cool} = (4 \pm 1) \times 10^{22}$ atoms cm^{-2}. This is enough to block most of the reverse shock emission at early times. This level of variable absorption is at tension ($\sim 2\sigma$ level) with the expected value Chevalier & Fransson (2003, pp. 171–194). This could be the result of excess absorption from partially ionized wind in the circumstellar material.

The amount of material in the cool shell depends upon the density of the ejecta which the reverse shock runs into. In a self similar explosion this depends on the circumstellar density and hence the mass loss rate from the progenitor (Chevalier & Fransson 2003, pp. 171–194). We find that the observed column density of cool material may be explained by a mass loss rate of $\dot{M} = (6 \pm 3) \times 10^{-6}\, M_{\odot}\ \mathrm{yr}^{-1}$. This is less precise than, but consistent with, the mass loss rate derived from the emission measure. This provides a consistency check for the scenario in which the excess absorption at early times indeed arises from the cooling shell.

5.4. Particle Acceleration

Electrons are accelerated in the strong forward shock produced by the SN. The optical photons produced by the SN are Inverse Compton scattered into the X-ray band by these relativistic electrons. Our measurement of the Inverse Compton flux density provides a direct probe of the particle acceleration efficiency.

Following Chevalier & Fransson (2006), we can express the Inverse Compton flux, for an electron index of $p = 3$, as

$$E\frac{dL_{\mathrm{IC}}}{dE} \approx 8.8 \times 10^{37} \gamma_{\mathrm{min}}\, \epsilon_{\mathrm{e}} \left(\frac{\dot{M}/\left(4\pi v_{\mathrm{w}}\right)}{5 \times 10^{11}\ \mathrm{g\ cm^{-1}}}\right) \times \left(\frac{V_{\mathrm{cs}}}{10^{4}\ \mathrm{km\ s^{-1}}}\right)\left(\frac{L_{\mathrm{bol}}}{10^{42}\ \mathrm{erg\ s^{-1}}}\right) \times \left(\frac{t}{10\ \mathrm{days}}\right)^{-1} \mathrm{erg\ s^{-1}}, \quad (10)$$

where γ_{min} is the minimum Lorentz factor of the relativistic electrons and ϵ_{e} is the fraction of thermal energy given to relativistic electrons. Our measurement of the Inverse Compton flux density implies an electron acceleration efficiency of $\gamma_{\mathrm{min}}\, \epsilon_{\mathrm{e}} = 0.02 \pm 0.01$. This shows that for a $\gamma_{\mathrm{min}} = 2$, around 1% of the thermal energy is used to accelerate relativistic electrons.

6. DISCUSSION

Explosions of massive stars with extended hydrogen envelopes produce SN II. The cores of these stars undergo rapid evolution during the final millennium before collapse, as they burn elements with progressively higher atomic numbers. The outer layers of these stars, supported against gravity by the energy generation in the core, can only slowly adjust to these changes over a much longer Kelvin–Helmholtz timescale. Therefore, conditions at the surface of the star, including luminosity and mass loss rate, are not expected to reflect the rapid evolution taking place in the core during the last stages of stellar evolution. This paradigm has been called into question by recent observations of luminous outbursts and massive outflows observed months to years before certain SNe.

Our X-ray observations of SN 2013ej indicate a mass loss rate from the progenitor which remained steady in the last 400 years before explosion. Within the best constraints the mass loss rate is consistent with stellar evolution models and theoretical mass loss prescriptions. If theoretical mass loss rate predictions are to be trusted, our precise measurement of the mass loss rate can be used to derive a mass of $M_{\mathrm{ZAMS}} = 13.7 \pm 0.3\, M_{\odot}$. The statistical uncertainty in such a measurement rivals the most precise progenitor mass measurements. However, we need to address gaps in our understanding of mass loss from massive stars (Smith 2014) before we can quantify systematic errors and rely on the accuracy of such a measurement. The mass loss rate inferred here is larger than that observed by us in the Type II-P SN 2004dj (Chakraborti et al. 2012). The mass loss rate from the progenitor of the Type II-P SN 2011ja showed rapid variations in the final stages before explosion (Chakraborti et al. 2013; Andrews et al. 2015). No such variation is inferred for SN 2013ej and its steady mass loss rate is comparable to the higher end of mass loss rates inferred for SN 2011ja. Through our program of X-ray observations of nearby SNe, we hope to shed light on details of mass loss from massive stars both as a function of progenitor mass and lookback time before explosion.

SN 2013ej was caught much sooner after explosion than SN 2004dj or SN 2011ja thanks to timely *Swift* and *Chandra* observations. This allowed us to discover two interesting effects. Chevalier & Fransson (2003, pp. 171–194) postulated the presence of a cool shell which may obscure the reverse shock emission at early times. We not only see this effect but measure the column depth of this shell and confirm that it is consistent with the circumstellar density seen in emission. If we can measure this effect more precisely in the future, the combination of the same mass loss rate measured using absorption and emission may allow an independent determination of the distance to nearby SNe. Chevalier & Fransson (2006) had suggested that Inverse Compton scattering by relativistic electrons may be the dominant source of X-rays in some SNe. At early times, when the light of the SN 2013ej provides a bright source of seed photons, emission from this non thermal process is found to be comparable to those from thermal processes (see early XRT spectrum in Figure 2). We use this to measure the efficiency of relativistic electron acceleration. Our measurement provides a check for recent predictions of particle acceleration efficiencies in strong but non-relativistic shocks (Ellison et al. 2007; Bai et al. 2015; Park et al. 2015).

We have also considered the detectability of core collapse SNe in external galaxies in the harder X-ray bands. With the capability of *NuSTAR* (Harrison et al. 2013), SN 2013ej would have been detected in 6–10 keV band at a 3σ level with an exposure of 1 Ms, provided the SN was targeted immediately after discovery and classification. Thus only very young and very nearby SNe, e.g., within 2–3 Mpc can be realistically targeted for detections in the high energy bands in the near future.

We acknowledge the use of public data from the *Swift* data archive. This research has made use of data obtained using the *Chandra* X-ray Observatory through an advance Target of Opportunity program and software provided by the *Chandra* X-ray Center (CXC) in the application packages CIAO and ChIPS. Support for this work was provided by the National Aeronautics and Space Administration through *Chandra* Award Number G04-15076X issued by the *Chandra* X-ray Observatory Center, which is operated by the Smithsonian Astrophysical Observatory for and on behalf of the National Aeronautics Space Administration under contract NAS8-03060. We thank Naveen Yadav for MESA runs and the anonymous referee for useful suggestions. A.R. thanks the Fulbright Foundation for a Fulbright-Nehru Fellowship at

Institute for Theory and Computation (ITC), Harvard University, and the Director and staff of ITC for their hospitality during his sabbatical leave from Tata Institute of Fundamental Research. At Tata Institute this research is part of 12th Five Year Plan Project 12P-0261.

REFERENCES

Andrews, J. E., Krafton, K. M., Clayton, G. C., et al. 2015, arXiv:1509.06379
Arnaud, K. A. 2013, in AAS/High Energy Astrophysics Division, 13, #117.04
Asplund, M., Grevesse, N., Sauval, A. J., & Scott, P. 2009, ARA&A, 47, 481
Bai, X.-N., Caprioli, D., Sironi, L., & Spitkovsky, A. 2015, ApJ, 809, 55
Bersten, M. C., & Hamuy, M. 2009, ApJ, 701, 200
Bose, S., Sutaria, F., Kumar, B., et al. 2015, ApJ, 806, 160
Cash, W. 1979, ApJ, 228, 939
Cedrés, B., Cepa, J., Bongiovanni, Á., et al. 2012, A&A, 545, A43
Chakraborti, S., Ray, A., Smith, R., et al. 2013, ApJ, 774, 30
Chakraborti, S., Yadav, N., Ray, A., et al. 2012, ApJ, 761, 100
Chevalier, R. A. 1974, ApJ, 188, 501
Chevalier, R. A. 1982a, ApJ, 258, 790
Chevalier, R. A. 1982b, ApJ, 259, 302
Chevalier, R. A., & Fransson, C. 2003, in Supernovae and Gamma-Ray Bursters, Vol. 598, ed. K. Weiler (Berlin: Springer)
Chevalier, R. A., & Fransson, C. 2006, ApJ, 651, 381
de Jager, C., Nieuwenhuijzen, H., & van der Hucht, K. A. 1988, A&AS, 72, 259
Dhungana, G., Kehoe, R., Vinko, J., et al. 2015, arXiv:1509.01721
Dhungana, G., Vinko, K., Wheeler, J. C., et al. 2013, CBET, 3609, 4
Dwarkadas, V. V. 2014, MNRAS, 440, 1917
Ellison, D. C., Patnaude, D. J., Slane, P., Blasi, P., & Gabici, S. 2007, ApJ, 661, 879
Fraser, M., Maund, J. R., Smartt, S. J., et al. 2014, MNRAS, 439, L56
Harrison, F. A., Craig, W. W., Christensen, F. E., et al. 2013, ApJ, 770, 103
Heger, A., Fryer, C. L., Woosley, S. E., Langer, N., & Hartmann, D. H. 2003, ApJ, 591, 288
Hou, F., Goodman, J., Hogg, D. W., Weare, J., & Schwab, C. 2012, ApJ, 745, 198
Huang, F., Wang, X., Zhang, J., et al. 2015, ApJ, 807, 59
Kalberla, P. M. W., Burton, W. B., Hartmann, D., et al. 2005, A&A, 440, 775
Kellogg, E., Baldwin, J. R., & Koch, D. 1975, ApJ, 199, 299
Kim, M., Zheng, W., Li, W., et al. 2013, CBET, 3606, 1
Lee, M., Li, K. L., Wang, J.-W., et al. 2013, ATel, 5466, 1
Leonard, P. b. D. C., Pignata, G., Dessart, L., et al. 2013, ATel, 5275, 1
Margutti, R., Chakraborti, S., Brown, P. J., & Sokolovsky, K. 2013, ATel, 5243, 1
Margutti, R., Milisavljevic, D., Soderberg, A. M., et al. 2014, ApJ, 780, 21
Matzner, C. D., & McKee, C. F. 1999, ApJ, 510, 379
Mauerhan, J. C., Smith, N., & Filippenko, A. V. 2013, MNRAS, 430, 1801
Mauron, N., & Josselin, E. 2011, A&A, 526, A156
McKee, C. F. 1974, ApJ, 188, 335
Nieuwenhuijzen, H., & de Jager, C. 1990, A&A, 231, 134
Nymark, T. K., Fransson, C., & Kozma, C. 2006, A&A, 449, 171
Ofek, E. O., Sullivan, M., Cenko, S. B., et al. 2013, Natur, 494, 65
Park, J., Caprioli, D., & Spitkovsky, A. 2015, PhRvL, 114, 085003
Pastorello, A., Cappellaro, E., Inserra, C., et al. 2013, ApJ, 767, 1
Paxton, B., Bildsten, L., Dotter, A., et al. 2011, ApJS, 192, 3
Richmond, M. W. 2014, JAVSO, 42, 333
Sanders, N. E., Soderberg, A. M., Gezari, S., et al. 2015, ApJ, 799, 208
Smartt, S. J., Eldridge, J. J., Crockett, R. M., & Maund, J. R. 2009, MNRAS, 395, 1409
Smith, N. 2014, ARA&A, 52, 487
Smith, N., Miller, A., Li, W., et al. 2010, AJ, 139, 1451
Smith, R. K., Brickhouse, N. S., Liedahl, D. A., & Raymond, J. C. 2001, ApJL, 556, L91
Valenti, S., Sand, D., Howell, D. A., et al. 2013, CBET, 3609, 1
Valenti, S., Sand, D., Pastorello, A., et al. 2014, MNRAS, 438, L101
Valenti, S., Sand, D., Stritzinger, M., et al. 2015, MNRAS, 448, 2608
Waagen, E. O., Cook, M., Harris, B., et al. 2013, CBET, 3609, 3
Weaver, T. A., Zimmerman, G. B., & Woosley, S. E. 1978, ApJ, 225, 1021
Wilms, J., Allen, A., & McCray, R. 2000, ApJ, 542, 914